






Article

Operando XAFS and XRD Study of a Prussian Blue Analogue Cathode Material: Iron Hexacyanocobaltate

Angelo Mullaliu ¹, Paolo Conti ², Giuliana Aquilanti ³, Jasper Rikkert Plaisier ³,
Lorenzo Stievano ^{4,5} and Marco Giorgetti ^{1,*}

¹ Department of Industrial Chemistry “Toso Montanari”, University of Bologna, Viale Risorgimento 4, 40136 Bologna, Italy; angelo.mullaliu2@unibo.it

² School of Science, Chemistry Division, University of Camerino, Via S. Agostino 1, 62032 Camerino, Macerata, Italy; paolo.conti@unicam.it

³ Elettra–Sincrotrone Trieste, ss 14, km 163.5, 34149 Basovizza, Trieste, Italy; giuliana.aquilanti@elettra.eu (G.A.); jasper.plaisier@elettra.eu (J.R.P.)

⁴ Institut Charles Gerhardt Montpellier, CNRS UMR 5253, Université de Montpellier, 34090 Montpellier, France; lorenzo.stievano@umontpellier.fr

⁵ Réseau sur le Stockage Electrochimique de l’Energie (RS2E), CNRS FR3459, 80090 Amiens, France

* Correspondence: marco.giorgetti@unibo.it; Tel.: +39-051-209-3690

Received: 9 October 2018; Accepted: 23 October 2018; Published: 25 October 2018



Abstract: The reversible electrochemical lithiation of potassium iron hexacyanocobaltate (FeCo) was studied by operando X-ray diffraction (XRD) and X-ray absorption fine structure (XAFS) assisted by chemometric techniques. In this way, it was possible to follow the system dynamics and retrieve structural and electronic transformations along cycling at both Fe and Co sites. These analyses confirmed that FeCo features iron as the main electroactive site. Even though the release of potassium ions causes a local disorder around the iron site, the material exhibits an excellent structural stability during the alkali ion deinsertion/insertion processes. An independent but interrelated analysis approach offers a good strategy for data treatment and provides a time-resolved picture of the studied system.

Keywords: battery; XRD; XAFS; EXAFS; MCR-ALS; operando

1. Introduction

The development of sustainable energy sources and the storage of electrical energy is a worldwide concern [1]. The call for an efficient electrochemical energy storage is answered by rechargeable batteries, which are based on high rate reaction of lithium ions into nano- and microstructured insertion materials [2–6]. Prussian blue analogues (PBAs), and in particular, metal hexacyanoferrates, have gained considerable attention as insertion type materials due to the ease of preparation, effectiveness as electrode materials, and wide versatility towards several ions [7–12]. The structure of such compound is characterized by a three-dimensional cubic network (although other crystal symmetries are found) of repeating $-\text{Fe}-\text{CN}-\text{M}-\text{NC}-$ units, where iron and M sites are typically octahedrally coordinated. The sites at the cube center (8c positions) can be occupied by countercations and water molecules to achieve charge neutrality. The lattice is characterized by zeolitic channels of roughly 3.2 Å, beyond cavities of around 5 Å arising from vacancies, allowing a facile (de)insertion of ions with little lattice strain. These structural features, together with the electroactivity of the constituting metals, form the basis for a vast range of applications, for instance, analyte sensors [13,14], magnetic devices [15], electrochromism [16], charge storage [17], supercapacitors [18,19], ion-exchange sieves [20,21], and even antibacterial agents against *Escherichia coli* and *Staphylococcus aureus* [22].

Since the performance of battery materials derives from a combination of structural and electronic properties and their reversible evolution along cycling, the investigation of such features and the comprehension of limiting or irreversible steps are of great technological importance to better design stable electrode materials [23]. However, the understanding of the redox and structural principles ruling the reaction mechanism is a difficult achievement, and sometimes erroneously taken for granted. For instance, the electroactivity of copper in a copper-hexacyanoferrate-based electrode in a battery system was recently unveiled [24], even though previous highly quoted literature had been sustaining a different mechanism [25]. The complexity of a battery, which consists of different components and various contributions to the overall redox process, could be untangled by using a combined complementary multitechnique approach. X-ray diffraction (XRD) is commonly used to identify crystalline phases, and to follow their modification during cycling [26–28]. X-ray absorption fine structure (XAFS) is the technique of choice for retrieving electronic and short-range structural information in transition-metal-based systems [29,30], by analyzing both X-ray absorption near-edge structure (XANES) and extended X-ray absorption fine structure (EXAFS) portions. Moreover, operando measurements allow a continuous monitoring of the system dynamics [31]; however, the acquired large datasets make necessary an advanced data treatment, often supported by chemometric techniques, such as multivariate curve resolution refined by alternating least squares (MCR-ALS) [32]. The complementary assistance of MCR-ALS might reveal the occurrence of complex multicomponent reactions, making the EXAFS interpretation more reliable.

In the present work, we propose a combined analysis of the electrochemical reversible lithiation of a potassium iron hexacyanocobaltate (FeCo). FeCo belongs to the class of PBAs, which have attained attention as insertion-type materials due to the highly reversible ion-insertion/deinsertion processes and stable cycle life [9,25].

2. Results

In the following subsections, we present the main results that allowed a deep understanding of the studied system.

2.1. XRD Data Analysis

The stoichiometry of the resulting FeCo can be written as $K_{0.44}Fe_{1.56}Co(CN)_6$ after XRF analysis, which provided a K/Fe/Co ratio of 0.44/1.56/1. The obtained pattern for the as-synthesized FeCo, depicted in Figure 1, well matches the reported model [33]. The refinement on the powder pattern led to a cubic structure (space group: $Fm\bar{3}m$) characterized by the lattice parameter $a = 10.224 \text{ \AA}$. The amounts of interstitial potassium (8c Wyckoff position) and structural iron (4b Wyckoff position) were refined leading to 0.4 K/Co and 1.4 Fe/Co ratios, in agreement with the stoichiometry. The resulting $[Co(CN)_6]^{3-}$ vacancies can be thus approximated to 29%, which is in line with the experimental value of 36%. During the redox reaction, the lattice space group ($Fm\bar{3}m$) did not change, however, the lattice dimension was affected by the process, as displayed in Figure 1. Here, the cubic lattice parameter evolution is overlapped with the potential profile during the electrochemical reaction. The lattice parameter for the pristine electrode ($a = 10.171 \text{ \AA}$) differs from that derived from the powder, since the electrode was dehydrated before use, manifesting a negative thermal expansion effect [34]. Figure 1b displays the charge/discharge electrochemical curve, evidencing an ion release and insertion capability of the studied material. The FeCo-based cathode was able to extract 0.51 K-equivalents in the charge process, while 0.54 Li-equivalents were inserted in the following discharge. However, the calculated amount of K^+ ions exceeded the stoichiometric one, so that we might attribute at least 0.07 ion-equivalents to side reactions in the charge process. Except for the initial part of the cycling, the lattice slightly shrank during the deinsertion of K^+ , whereas Li^+ insertion provoked a relative expansion, which was, however, limited to less than 0.6%. The negligible lattice strain exhibited by FeCo is indeed a common characteristic of PBA materials. Furthermore, the refinement suggests that ion insertion most likely occurred along the (220) plane (cf. Supplementary Materials).

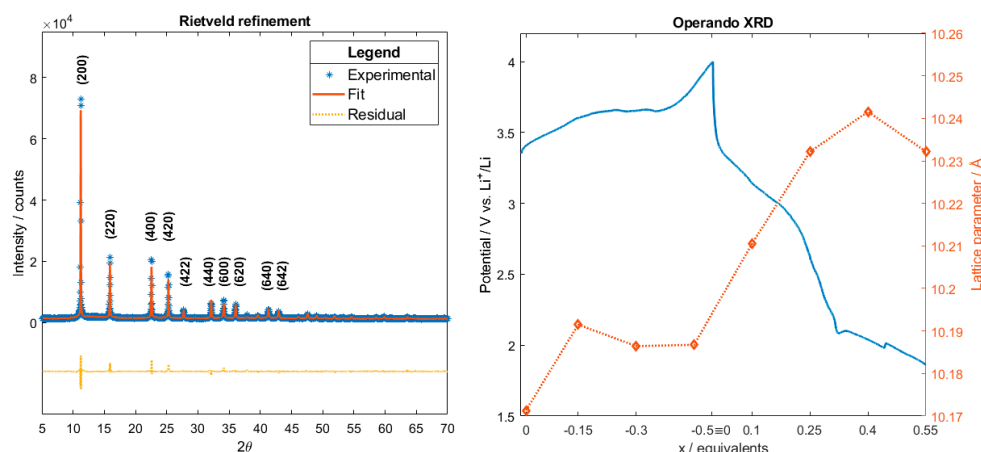


Figure 1. On the left side, the Rietveld refinement on FeCo powder is presented. The most relevant Miller planes are indexed in brackets. On the right side, the operando XRD electrochemical profile (blue line) and concomitant lattice parameter evolution (red scatter) are shown.

2.2. XANES Data Analysis

As previously reported [35,36] and indicated in Figure 2, release/insertion reaction induced a deep modification at the Fe K-edge, while the Co K-edge remained mostly unchanged. This highlights the electroactivity of the iron site with consequent electronic and structural adjustments. For instance, the Fe main edge shifted towards higher energies while charging, evidencing an oxidation of the metal, while the opposite trend was observed in the insertion process.

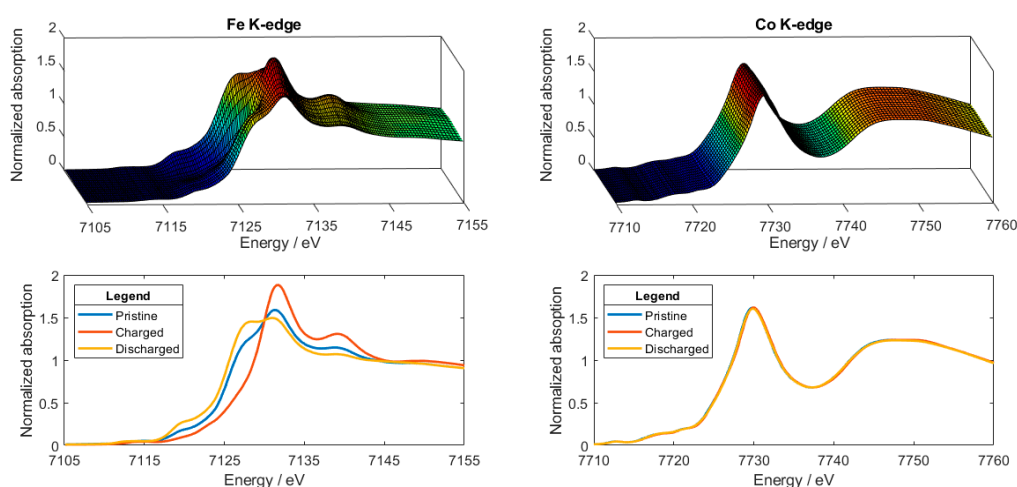


Figure 2. XAFS K-edge evolution for both iron (left) and cobalt (right). In the bottom layer, pristine, charged, and discharged states spectra are compared and presented for each metal site. The figure has been adapted from reference [35].

XANES analysis was performed by using a chemometric approach. MCR-ALS provides an additive bilinear model of pure contributions without any preexisting model or a priori information on the system, decomposing the operando data matrix $X_{S,W}$ in a product of two matrices to which chemical meaning can be attributed [32,37], as it follows Equation (1):

$$X_{S,W} = C_{S,F} \cdot A_{W,F}, \quad (1)$$

where $C_{S,F}$ contains the pure concentration profiles and $A_{W,F}$ the pure spectral components.

In this case, the MCR-ALS algorithm was applied to the whole series of operando Fe K-edge XANES spectra because of the higher variability along the W columns of the experimental $X_{S,W}$ matrix.

In Figure 3a,b, the concentration profiles ($C_{S,F}$) and the pure spectral components ($A_{W,F}$) are reported, respectively. The overall results of the chemometric analysis can be sorted as: (i) a transformation during charge that can be approximated to the conversion of species 1 to species 2, while the system evolves to species 3 in the following discharge process [36]; (ii) the concentration profile does not significantly evolve during the first 0.3 extracted ion-equivalents, after which the redox reaction approaches a pseudo-zero-order kinetics; (iii) the pristine species does not entirely match with the first pure spectral component, however, they have a likeness of 74%. As previously discussed [35], the first part of the charge process (panel c) assumes a curved shape, which was attributed to an irreversible dehydration process of the pristine electrode. Consequently, the first 0.3 K-equivalents should be considered not extracted from FeCo in this initial stage and ascribed to a parasite reaction, thus explaining the flat concentration profile. Taking into account this last point, 0.62 K^+ were extracted, while 0.62 Li^+ were inserted during the following discharge. Again, the amount of deinserted K^+ ions exceeded the stoichiometric value, so that in total at least 0.47 ion-equivalents were attributable to side reactions in the charge process. Moreover, to confirm that the pristine species is in fact a combination of more contributions, we carried out an independent linear combination fitting: panel d illustrates the additive contributions at the Fe K-edge of the fully charged (33%) and discharged states (67%). According to this result, the pristine Fe species possesses an oxidation state close to approximately (+2.3). FeCo has to be considered a mixed-valence compound as many other PBAs, therefore the $(FeCo)^{Ox}$ notation adopted by Berrettoni et al. [38,39] to describe the overall oxidation number of the metals appears to be the most appropriate way to refer to this class of materials.

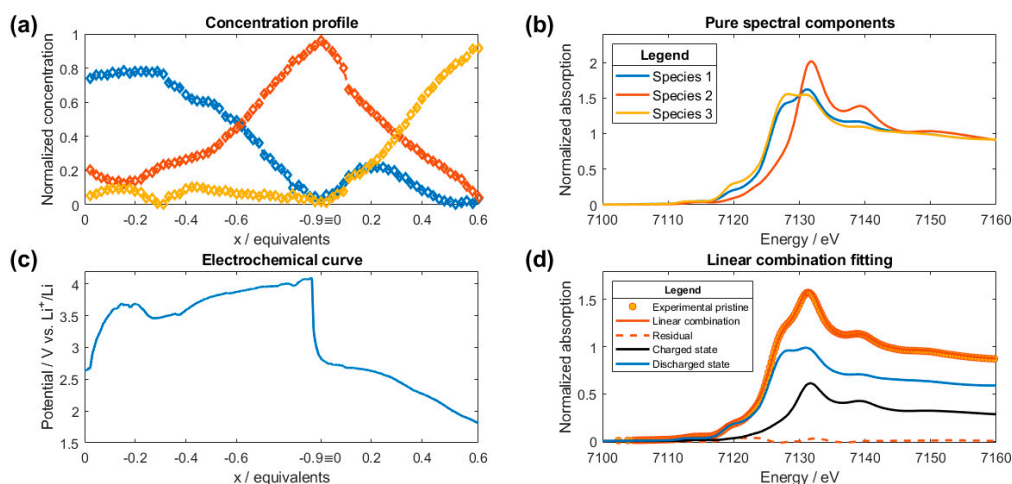


Figure 3. MCR-ALS analysis results: (a) concentration profile; (b) pure spectral components. In panel (c), the electrochemical potential profile is reported, while the linear combination fit on the pristine sample is illustrated in panel (d). The MCR-ALS results have been adapted from reference [36].

To complement the analysis on the XANES spectra, an independent pre-edge data treatment was performed at the Fe K-edge. The pre-edge region was fitted with a sum of Gaussian functions by first subtracting a spline function background to the normalized spectra, defined by selecting an appropriate number of anchor points in the 7105–7125 eV window. Despite the considered approximations, the results are noteworthy. As reported in Figure 4, the pre-edge displays different features which were separately fitted. The number of Gaussian components used to obtain a reasonable fit was kept as low as possible to reduce the amount of refinable parameters, and it varied from two to four to consider all contributions (cf. Supplementary Materials). Interestingly, the peak centered at 7119 eV diminished in intensity during K^+ deinsertion, while it increased in intensity during discharge. This rising-edge feature arises from normally forbidden dipole transitions to empty bound states involving the breakdown of the octahedral symmetry of ordered atomic shells beyond the

cyanides [40–42]. More details on the fitting results and the exact correspondence of the displayed states with the collected spectra can be found in the Supplementary Materials.

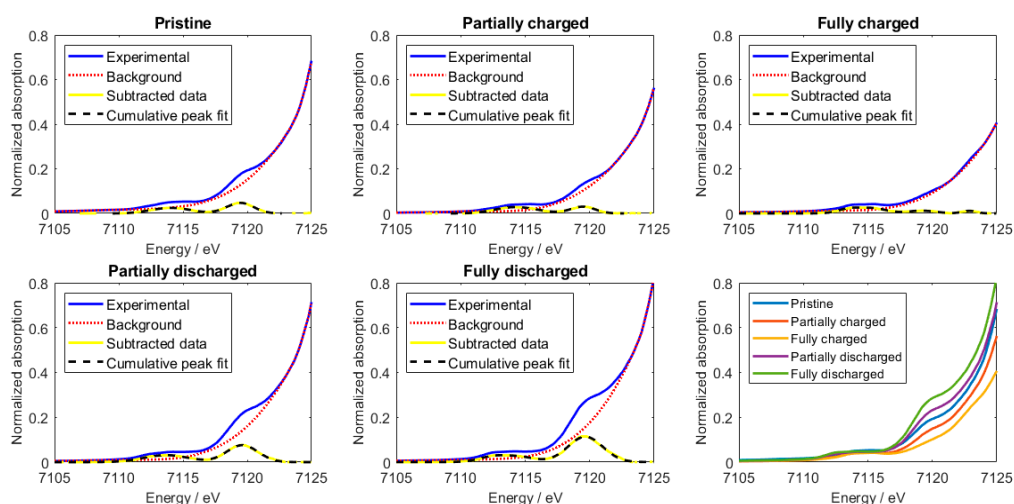


Figure 4. Pre-edge data analysis for the pristine, partially charged, fully charged, partially discharged, fully discharged states, and their comparison.

2.3. EXAFS Data Analysis

Complementary structural information about both Fe and Co sites can be extracted from the EXAFS signals. Analysis of the pristine electrode was first done to check the reliability of the structural model as well as to set the relevant parameters for the minimization. In a second moment, the analysis was extended to the operando dataset. For an accurate extraction of the structural information, all the measurements were analyzed by multiple-edge approach [43], that is, a simultaneous fitting procedure at both Fe and Co metal edges. This in turns means that the same structural parameters are probed using two independent measurements, hence the reliability of the fitting minimization is enhanced. Figure 5 displays the details of the EXAFS analysis for the pristine, partially charged, fully charged, partially discharged, fully discharged states at Fe (top layer) and Co (bottom layer) K-edges. Briefly, (i) only few relevant single EXAFS contributions were necessary to simulate the overall EXAFS signal at each edge; (ii) not only the two-body signals, but also the three- and the four-body MS terms are relevant with intensities comparable to the first shell; (iii) the two-body Fe-M^{8c} and Co-M^{8c} signals depend on the cation occupancy during charge and discharge, explaining the reduced intensities observed for fully charged states; (iv) the multi-edge refinement allows one to take into consideration the oscillation of the MS terms at the Fe K-edge that could overlay the Co K-edge.

The fit was performed on a representative selection of spectra by taking into account the XANES traces and the result of the MCR-ALS analysis. The most relevant fitting results are displayed in Figure 6. Here, the difference in the trends displayed in panels a and b is noteworthy. Indeed, even though bond distances were not significantly altered in the process, the disorder related to Fe–N bonds increased considerably near the fully charged state, that is, the state with all interstitial ions deinserted. On the other side, the Co–C fragment was neither electronically (as observed by the XANES of Figure 2) nor structurally affected by the electrochemical reaction. Additionally, the number of linear Fe–NC–Co chains, labelled as CN^{chain}, set the degeneracy of the Fe–NC–Co fragments and therefore can be considered as an indicator of the linearity of the chain (this is due to the strong focusing effect of the linear Co–C–N and of the additional superfocusing one carried out by the linear Co–C–N–Fe fragment). As seen from panel c, the CN^{chain} parameter oscillated around a value of 3.5 during charge, while its centroid slightly decreased in the discharge. Although the large error bars set a limit to further considerations, we might assume that the lithiation could induce a small deviation from the linearity of the orthogonal chains. Finally, the Fe coordination number to the interstitial

cation decreased as the latter was deinserted, while it was experiencing a slight rising trend during the discharge (panel d). The number quoted for this parameter can only be considered qualitative. The observed trend corresponds well to the cation interstitial occupancy in the electrochemical reaction.

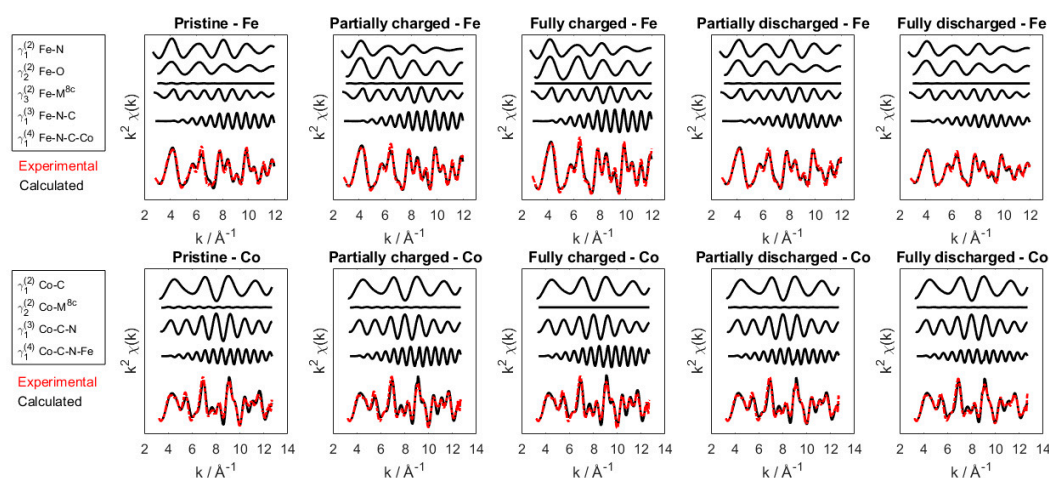


Figure 5. MS contributions and best fit for the pristine, partially charged, fully charged, partially discharged, fully discharged states at Fe (first layer) and Co (second layer) K-edge.

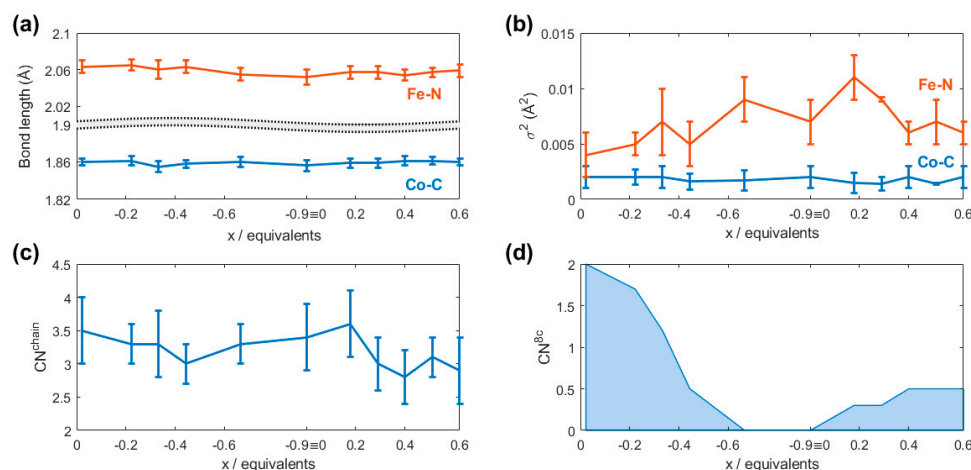


Figure 6. Relevant EXAFS fitting results: (a) first shell distances behavior: Fe–N and Co–C; (b) EXAFS Debye–Waller factors; (c) variation in Fe–N–C–Co chains degeneracy during lithiation; (d) variation in the coordination number of the 8c interstitial cation.

The results of the fitting of the EXAFS spectra, in terms of relevant bond lengths, Debye–Waller factors, and coordination numbers, are reported in Table 1. In addition, the table indicates the released fitting quotation for $S_0^2(\text{Fe})$ and $S_0^2(\text{Cu})$ in the pristine sample, which were consequently kept fixed regarding the analysis of the lithiated samples. The geometric half-cell parameter ($a/2$) was derived as sum of the Fe–N–C–Co fragment distances.

Table 1. EXAFS fitting results. Results for powder, pristine, and cycled samples are reported. Please refer to the Supplementary Materials for the correspondence between spectra number and cycling advancement.

	Powder	Pristine	C10	C15	C20	C30	C42	C50	C55	C60	C65	C70
Co-C (N)/Å	1.862(3)	1.860(4)	1.861(5)	1.855(6)	1.858(4)	1.860(5)	1.856(6)	1.859(5)	1.859(5)	1.861(5)	1.861(4)	1.860(4)
σ^2 Co-C/Å ²	0.0016(5)	0.002(1)	0.0020(7)	0.002(1)	0.0016(7)	0.0017(9)	0.002(1)	0.002(1)	0.0015(9)	0.0014(6)	0.002(1)	0.0014(7)
C≡N/Å	1.187(5)	1.185(5)	1.187(7)	1.18(1)	1.18(1)	1.182(7)	1.184(7)	1.183(6)	1.182(6)	1.184(6)	1.184(7)	1.186(6)
σ^2 C≡N/Å ²	0.007(2)	0.005(2)	0.0013(6)	0.005(2)	0.003(1)	0.002(1)	0.002(1)	0.006(2)	0.005(2)	0.0012(4)	0.004(2)	0.004(1)
Fe-N/Å	2.077(8)	2.063(7)	2.065(6)	2.06(1)	2.063(7)	2.055(7)	2.052(8)	2.057(7)	2.057(7)	2.054(6)	2.057(5)	2.059(7)
σ^2 Fe-N/Å ²	0.007(2)	0.004(2)	0.005(1)	0.007(3)	0.005(2)	0.009(2)	0.007(2)	0.011(2)	0.009(2)	0.006(1)	0.007(2)	0.006(1)
Fe-O/Å	2.09(2)	2.02(1)	2.02(2)	2.03(1)	2.036(8)	2.015(9)	2.00(1)	2.008(8)	2.009(9)	2.02(1)	2.02(2)	2.02(1)
σ^2 Fe-O/Å ²	0.006(3)	0.005(3)	0.004(2)	0.004(2)	0.002(1)	0.003(2)	0.003(2)	0.002(1)	0.003(1)	0.006(2)	0.004(1)	0.005(2)
σ^2 Co-C-N/deg ²	4(3)	4(3)	4(2)	4(3)	4(3)	4(3)	4(3)	4(3)	5(4)	4(3)	4(3)	5(4)
σ^2 Fe-N-C/deg ²	9(6)	10(8)	10(8)	3(2)	10(9)	10(8)	9(8)	9(8)	9(8)	9(8)	9(8)	9(8)
E ₀ (Fe)/eV	7121.4(6)	7123.4	7123.2	7123.7	7124.2	7124.3	7124.9	7124.3	7123.7	7123.5	7122.9	7122.4
E ₀ (Co)/eV	7717.8(6)	7717.5	7718.4	7717.2	7717.3	7717.4	7717.2	7717.3	7717.3	7717.4	7717.4	7717.4
CN ^{chain}	3.5(3)	3.5(5)	3.3(3)	3.3(5)	3.0(3)	3.3(3)	3.4(5)	3.6(5)	3.0(4)	2.8(4)	3.1(3)	2.9(5)
CN3 (Fe-O)	1.8(5)	1.9(3)	2.0(4)	2.2(3)	2.2(3)	2.7(3)	2.9(4)	2.6(3)	2.6(3)	2.4(3)	2.0(3)	2.3(4)
CN ^{8c} (M ^{8c} = K) ¹	FIX 2	FIX 2	1.7	1.2	0.5	0	0	0.3	0.3	0.5	0.5	0.5
S ₀ ² (Fe)	0.66(4)	0.65(4)	0.66(3)	0.66(4)	0.66(3)	0.65(3)	0.66(3)	0.65(3)	0.66(3)	0.66(3)	0.69(6)	0.65(3)
S ₀ ² (Co)	0.71(3)	0.76(4)	0.77(4)	0.73(3)	0.72(3)	0.74(3)	0.73(4)	0.78(4)	0.72(4)	0.72(3)	0.73(3)	0.72(3)
a/2/Å ²	5.12	5.1	5.11	5.1	5.1	5.09	5.09	5.1	5.1	5.1	5.1	5.1
10 ⁶ χ ² -like residual	3.63	5.83	5.91	5.8	5.72	6.5	7.22	6.02	5.34	4.95	4.98	4.44

¹ During lithiation process, potassium was still considered to obtain a qualitative trend, since Li⁺ ions slightly contribute to the scattering signal. ² Data obtained from geometrical evaluation.

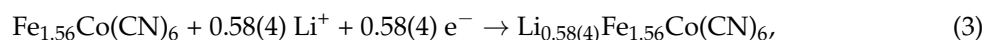
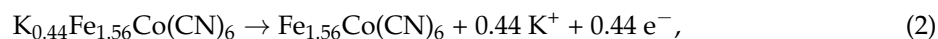
3. Discussion and Conclusions

The structural adjustments of the lattice of FeCo were measured via XRD, which probed the material long-range order and retrieved the atomic positions during cycling, confirming an excellent structural retention during the release/insertion processes. Indeed, the *Fm3m* cubic lattice host is preserved through the whole operando experiment, with interstitial ions occupying and being extracted from 8c lattice sites. The low strain (<0.6% variation in lattice parameter during charge/discharge) demonstrates the structural stability of the material upon the first cycle.

The electronic counterpart was studied via XAFS, which portrayed iron as the main electroactive metal. The MCR-ALS chemometric analysis of the operando XANES data was successfully employed to reconstruct the pure spectral components and to follow their respective contribution during cycling, giving further insight into process dynamics. The parasite dehydration process contributes to the irreversible charge capacity, and is not observed in the case of the previously dehydrated operando XRD sample. Independent analyses based on linear combination fitting and pre-edge region fitting were carried out to complement and validate the obtained results. Pristine FeCo differs from fully charged and discharged states, but can be described by their linear combination.

The short-range order and structural evolution were investigated by analyzing the EXAFS spectra through a multiple-edge refinement approach. While the cobalt centers are not significantly altered by the redox process, the disorder associated to the Fe–N bond increases remarkably in the oxidized state. Moreover, the linearity of the Fe–NC–Co chains is slightly altered by lithium insertion, while the interstitial cation occupancy is strictly related to the state of charge of the material.

In summary, the following reactions are proposed in a first approximation for charge (Equation (2)) and discharge (Equation (3)), in the case of a dehydrated structure:



where the number in parentheses indicates the estimated error on lithium equivalents, according to the discussed operando measurements.

4. Materials and Methods

The sample was prepared by coprecipitation method at 40 °C, as previously reported [43]. The electrodes for the operando XAFS measurements were obtained by tape casting a slurry containing the 80% of pure active material (AM), 10% polyvinylidene fluoride (PVDF), and 10% carbon black (CB) in *N*-methylpyrrolidone (NMP) on a flat polytetrafluoroethylene (PTFE) surface, while the electrodes for operando XRD experiments were obtained by thoroughly mixing the pure AM (70%), 10% CB, and 10% vapor-grown carbon fibers high density (VGCF-H) in an agate mortar; 10% PTFE was finally added and mixing continued until a homogenous paste was obtained. Obtained mass loadings were about 6–8 mg/cm² of AM. A suitable electrochemical cell for in situ experiments, described in detail elsewhere [44], was used during both XRD and XAFS measurements. The cell consisted of a large piece of lithium metal foil, adopted as negative electrode, while processed FeCo was used as positive electrode. 1M LiPF₆ in an ethylene carbonate, propylene carbonate, dimethyl carbonate 1:1:3 volumetric mixture (EC:PC:3DMC) served as electrolyte solution. Positive electrode, Celgard separator soaked in the electrolyte, and negative electrode was stacked and assembled under inert atmosphere in an Ar-filled glove-box. The electrode employed in the operando XRD measurement was thermally treated before use, dehydrating at 80 °C under vacuum overnight.

XRD and XAFS experiments were performed at Elettra Sincrotrone in Basovizza (Italy), at the MCX [45] and XAFS beam line [35], respectively. The storage ring operated at 2.0 GeV in top-up mode with a typical current of 300 mA.

XRD data were collected using a monochromatic X-ray beam of 1 Å. The XRD pattern of the FeCo powder sample was recorded in a capillary geometry, setting the spinner at 300 revolutions per minute, and acquiring the diffractogram consecutively in the $5^\circ < 2\theta < 70^\circ$ range, with steps of 0.01° and an acquisition time of 1 s per step. Operando data were instead collected in the flat plate mode consecutively from 10° to 30° 2θ range with a 0.01° step and 0.5 s/point acquisition time.

XAFS data were collected at Fe and Co K-edges in transmission mode using ionization chambers filled with a mixture of Ar, N₂, and He to have 10%, 70%, and 95% of absorption in the I₀, I₁, and I₂ chambers, respectively. An internal reference of iron and cobalt foil was used for energy calibration in each scan. This allowed a continuous monitoring of the energy during consecutive scans. No energy drifts of the monochromator were observed during the experiments. Spectra at Fe and Co K-edges were collected with a constant k-step of 0.03 \AA^{-1} with 2 s/point acquisition time. Data were collected from 6900 eV to 8320 eV at the Fe and Co K-edges. The energies were calibrated by assigning the first inflection point of the spectra of the metallic iron and cobalt to 7112 eV and 7709 eV, respectively. The white beam was monochromatized using a fixed-exit monochromator equipped with a pair of Si(111) crystals. Harmonics were rejected by using the cutoff of the reflectivity of the platinum mirror placed at 3 mrad with respect to the beam upstream of the monochromator and by detuning the second crystal of the monochromator by 30% of the maximum. In situ data were acquired during the first charge to 4.0 V vs. Li⁺/Li and subsequent discharge to 1.8 V vs. Li⁺/Li at C/34 and C/31 current rates for operando XRD and XAFS, respectively, by considering 1C rate equals to the current needed to insert one equivalent of Li-ion per formula unit (in the charged state) in one hour, thus a theoretical specific capacity of 88 mAh g⁻¹. The equivalents of reacted ions (or better, exchanged electrons) have been calculated from the imposed value of current and the elapsed time in the operando measurement.

Rietveld refinement was carried out on XRD patterns using FullProf Suite software [46] and assuming as structural model the one reported by Mullica et al. [33]. A pseudo-Voigt function was adopted for peak shape. Peaks corresponding to PTFE (contained in the electrode formulation) were not refined, excluding the corresponding regions, that is, $11.60\text{--}11.95^\circ$ and $16.78\text{--}17.31^\circ$ [47]. Also, the $29.31\text{--}29.43^\circ$ region was not considered, due to the presence of the beryllium peak arising from the in situ cell window. Graphical representation of structures was exploited by means of VESTA software [48].

XAFS spectra were pretreated and calibrated using the Athena program [49]. The pre-edge background was removed by subtracting a linear function extrapolated from the pre-edge region, and the XANES spectra were normalized at the unity by extrapolation of the atomic background.

The EXAFS analysis was performed using the GNXAS package [50,51] which is based on the MS theory. The method uses the decomposition of the EXAFS signals into a sum of several contributions, namely the n-body terms. The theoretical signal is calculated ab initio and contains the relevant two-body $\gamma^{(2)}$, three-body $\gamma^{(3)}$, and four-body $\gamma^{(4)}$ MS terms [52]. The two-body terms are associated with pairs of atoms, and probe their distances and variances. The three-body terms are associated with triplets of atoms and probe angles, and bond–bond and bond–angle correlations. The four-body terms are associated to chains of four atoms, and probe distances and angles in-between, and bond–bond and bond–angle correlations. However, because of the linearity of the Fe–N–C–Co chains, all the angles were set to be 180° , hence the actual number of parameters used to define the $\gamma^{(3)}$ or the $\gamma^{(4)}$ peak was reduced by symmetry. More details on the use of parameters correlation in the four-body term is out of the aim of the present work and can be found in the references [43,53]. Data analysis was performed by minimizing an χ^2 -like residual function that compares the theoretical (model) signal, $\mu_{\text{mod}}(E)$, to the experimental one, $\mu_{\text{exp}}(E)$. The phase shifts for the photoabsorber and backscatterer atoms were calculated starting from the structure reported by Mullica et al. [33] according to the muffin-tin approximation and allowing 10% overlap between the muffin-tin spheres. The Hedin–Lundqvist complex potential [54] was used for the exchange–correlation potential of the excited state. The core-hole lifetime, Γ_c , was fixed to the tabulated value [55] and was included in

the phase shift calculation. The experimental resolution used in the fitting analysis was around 1 eV, in agreement with the stated value for the beam line used.

Supplementary Materials: The following are available online at <http://www.mdpi.com/2410-3896/3/4/36/s1>, Figure S1: Rietveld refinement on the 60th XRD pattern: (a) 8c position not refined and (b) refined. Note the fit improvement at (220) plane. Figure S2: Comparison between: (a) pristine state and first spectral component; (b) charged state and second spectral component; (c) discharged state and third spectral component. Figure S3: Pre-edge fitting analysis for the (a) 1th; (b) 30th; (c) 42nd; (d) 60th; (e) 70th spectra. Figure S4: *Operando* XAFS electrochemical profile (blue line) and concomitant 7119 eV peak area evolution (red scatter) are shown. Table S1: Correspondence between Miller planes and 2θ angles. Table S2: Correspondence between collected pattern number and extracted/inserted ion equivalents. Table S3: Correspondence between collected spectrum number and extracted/inserted ion equivalents.

Author Contributions: Conceptualization, M.G.; methodology, M.G., L.S., G.A., and J.R.P.; data acquisition, G.A., J.R.P., A.M., L.S., and M.G.; data analysis, A.M., P.C., M.G.; writing—original draft preparation, A.M., M.G.; writing—review and editing, all co-authors.; supervision, M.G.; project administration, M.G.; funding acquisition, M.G.

Funding: This research was funded by the Università di Bologna, RFO grant, while XAFS and XRD measurements at Sincostrone Elettra were supported by the 20145337 and 20155185 projects, respectively (MG as PI).

Acknowledgments: Marcus Fehse is gratefully acknowledged for technical help in cell preparation and XAFS data collection. Robert Dominko is gratefully thanked for the access to his laboratory at KI, Ljubljana (Slovenia).

Conflicts of Interest: The authors declare no conflict of interest.

References

1. Chu, S.; Majumdar, A. Opportunities and challenges for a sustainable energy future. *Nature* **2012**, *488*, 294–303. [[CrossRef](#)] [[PubMed](#)]
2. Goodenough, J.B.; Kim, Y. Challenges for rechargeable Li batteries. *Chem. Mater.* **2010**, *22*, 587–603. [[CrossRef](#)]
3. Sun, H.; Wang, J.G.; Zhang, Y.; Hua, W.; Li, Y.; Liu, H. Ultrafast lithium energy storage enabled by interfacial construction of interlayer-expanded MoS₂/N-doped carbon nanowires. *J. Mater. Chem. A* **2018**, *6*, 13419–13427. [[CrossRef](#)]
4. Liu, H.; Wang, J.G.; Hua, W.; Wang, J.; Nan, D.; Wei, C. Scale-up production of high-tap-density carbon/MnOx/carbon nanotube microcomposites for Li-ion batteries with ultrahigh volumetric capacity. *Chem. Eng. J.* **2018**, *354*, 220–227. [[CrossRef](#)]
5. Goodenough, J.B.; Manthiram, A. A perspective on electrical energy storage. *MRS Commun.* **2014**, *4*, 135–142. [[CrossRef](#)]
6. Goodenough, J.B. Electrochemical energy storage in a sustainable modern society. *Energy Environ. Sci.* **2014**, *7*, 14–18. [[CrossRef](#)]
7. Wessells, C.D.; Peddada, S.V.; McDowell, M.T.; Huggins, R.A.; Cui, Y. The Effect of Insertion Species on Nanostructured Open Framework Hexacyanoferrate Battery Electrodes. *J. Electrochem. Soc.* **2012**, *159*, A98–A103. [[CrossRef](#)]
8. Moritomo, Y.; Urase, S.; Shibata, T. Enhanced battery performance in manganese hexacyanoferrate by partial substitution. *Electrochim. Acta* **2016**, *210*, 963–969. [[CrossRef](#)]
9. Song, J.; Wang, L.; Lu, Y.; Liu, J.; Guo, B.; Xiao, P.; Lee, J.J.; Yang, X.Q.; Henkelman, G.; Goodenough, J.B. Removal of Interstitial H₂O in Hexacyanometallates for a Superior Cathode of a Sodium-Ion Battery. *J. Am. Chem. Soc.* **2015**, *137*, 2658–2664. [[CrossRef](#)] [[PubMed](#)]
10. Wessells, C.D.; Peddada, S.V.; Huggins, R.A.; Cui, Y. Nickel hexacyanoferrate nanoparticle electrodes for aqueous sodium and potassium ion batteries. *Nano Lett.* **2011**, *11*, 5421–5425. [[CrossRef](#)] [[PubMed](#)]
11. Eftekhari, A. Potassium secondary cell based on Prussian blue cathode. *J. Power Sources* **2004**, *126*, 221–228. [[CrossRef](#)]
12. Liu, S.; Pan, G.L.; Li, G.R.; Gao, X.P. Copper hexacyanoferrate nanoparticles as cathode material for aqueous Al-ion batteries. *J. Mater. Chem. A* **2015**, *3*, 959–962. [[CrossRef](#)]
13. Giorgetti, M.; Scavetta, E.; Berrettoni, M.; Tonelli, D. Nickel hexacyanoferrate membrane as a coated wire cation-selective electrode. *Analyst* **2001**, *126*, 2168–2171. [[CrossRef](#)] [[PubMed](#)]

14. Giorgetti, M.; Tonelli, D.; Berrettoni, M.; Aquilanti, G.; Minicucci, M. Copper hexacyanoferrate modified electrodes for hydrogen peroxide detection as studied by X-ray absorption spectroscopy. *J. Solid State Electrochem.* **2014**, *18*, 965–973. [[CrossRef](#)]
15. Sato, O.; Iyoda, T.; Fujishima, A.; Hashimoto, K. Photoinduced magnetization of a cobalt-iron cyanide. *Science* **1996**, *272*, 704–705. [[CrossRef](#)] [[PubMed](#)]
16. Bueno, P.R.; Giménez-Romero, D.; Ferreira, F.F.; Setti, G.O.; Garcia-Jareño, J.J.; Agrisuelas, J.; Vicente, F. Electrochromic switching mechanism of iron hexacyanoferrates molecular compounds: The role of $\text{Fe}^{2+}(\text{CN})_6$ vacancies. *J. Phys. Chem. C* **2009**, *113*, 9916–9920. [[CrossRef](#)]
17. Neff, V.D. Some Performance Characteristics of a Prussian Blue Battery. *J. Electrochem. Soc.* **1985**, *132*, 1382. [[CrossRef](#)]
18. Wang, J.-G.; Zhang, Z.; Zhang, X.; Yin, X.; Li, X.; Liu, X.; Kang, F.; Wei, B. Cation exchange formation of prussian blue analogue submicroboxes for high-performance Na-ion hybrid supercapacitors. *Nano Energy* **2017**, *39*, 647–653. [[CrossRef](#)]
19. Wang, J.-G.; Zhang, Z.; Liu, X.; Wei, B. Facile synthesis of cobalt hexacyanoferrate/graphene nanocomposites for high-performance supercapacitor. *Electrochim. Acta* **2017**, *235*, 114–121. [[CrossRef](#)]
20. Chen, R.; Tanaka, H.; Kawamoto, T.; Asai, M.; Fukushima, C.; Kurihara, M.; Watanabe, M.; Arisaka, M.; Nankawa, T. Preparation of a film of copper hexacyanoferrate nanoparticles for electrochemical removal of cesium from radioactive wastewater. *Electrochem. Commun.* **2012**, *25*, 23–25. [[CrossRef](#)]
21. Ventura, M.; Mullaliu, A.; Ciurdac, D.E.; Zappoli, S.; Giuli, G.; Tonti, D.; Enciso, E.; Giorgetti, M. Thin layer films of copper hexacyanoferrate: Structure identification and analytical applications. *J. Electroanal. Chem.* **2018**, *827*, 10–20. [[CrossRef](#)]
22. Ciabocco, M.; Cancemi, P.; Saladino, M.L.; Caponetti, E.; Alduina, R.; Berrettoni, M. Synthesis and antibacterial activity of iron-hexacyanocobaltate nanoparticles. *J. Biol. Inorg. Chem.* **2018**, *23*, 385–398. [[CrossRef](#)] [[PubMed](#)]
23. Lee, Y.S.; Shin, W.K.; Kannan, A.G.; Koo, S.M.; Kim, D.W. Improvement of the Cycling Performance and Thermal Stability of Lithium-Ion Cells by Double-Layer Coating of Cathode Materials with Al_2O_3 Nanoparticles and Conductive Polymer. *ACS Appl. Mater. Interfaces* **2015**, *7*, 13944–13951. [[CrossRef](#)] [[PubMed](#)]
24. Mullaliu, A.; Aquilanti, G.; Conti, P.; Plaisier, J.R.; Fehse, M.; Stievano, L.; Giorgetti, M. Copper Electroactivity in Prussian Blue-Based Cathode Disclosed by Operando XAS. *J. Phys. Chem. C* **2018**, *122*, 15868–15877. [[CrossRef](#)]
25. Wessells, C.D.; Huggins, R.A.; Cui, Y. Copper hexacyanoferrate battery electrodes with long cycle life and high power. *Nat. Commun.* **2011**, *2*, 550. [[CrossRef](#)] [[PubMed](#)]
26. Allan, D.R.; Collins, S.P.; Evans, G.; Hall, D.; McAuley, K.; Owen, R.L.; Sorensen, T.; Tang, C.C.; von Delft, F.; Wagner, A.; et al. Status of the crystallography beamlines at Diamond Light Source. *Eur. Phys. J. Plus* **2015**, *130*, 1–20. [[CrossRef](#)]
27. Renman, V.; Ojwang, D.O.; Valvo, M.; Gómez, C.P.; Gustafsson, T.; Svensson, G. Structural-electrochemical relations in the aqueous copper hexacyanoferrate-zinc system examined by synchrotron X-ray diffraction. *J. Power Sources* **2017**, *369*, 146–153. [[CrossRef](#)]
28. Ojwang, D.O.; Grins, J.; Wardecki, D.; Valvo, M.; Renman, V.; Häggström, L.; Ericsson, T.; Gustafsson, T.; Mahmoud, A.; Hermann, R.P.; et al. Structure Characterization and Properties of K-Containing Copper Hexacyanoferrate. *Inorg. Chem.* **2016**, *55*, 5924–5934. [[CrossRef](#)] [[PubMed](#)]
29. Giorgetti, M. A Review on the Structural Studies of Batteries and Host Materials by X-Ray Absorption Spectroscopy. *ISRN Mater. Sci.* **2013**, *2013*, 938625. [[CrossRef](#)]
30. Buchholz, D.; Li, J.; Passerini, S.; Aquilanti, G.; Wang, D.; Giorgetti, M. X-ray Absorption Spectroscopy Investigation of Lithium-Rich, Cobalt-Poor Layered-Oxide Cathode Material with High Capacity. *ChemElectroChem* **2015**, *2*, 85–97. [[CrossRef](#)]
31. Giorgetti, M.; Stievano, L. *X-ray Absorption Spectroscopy Study of Battery Materials*, 1st ed.; InTech: Rijeka, Croatia, 2017; ISBN 978-953-51-3014-7.
32. Conti, P.; Zamponi, S.; Giorgetti, M.; Berrettoni, M.; Smyrl, W.H. Multivariate Curve Resolution Analysis for Interpretation of Dynamic Cu K-Edge X-ray Absorption Spectroscopy Spectra for a Cu Doped V_2O_5 Lithium Battery. *Anal. Chem.* **2010**, *82*, 3629–3635. [[CrossRef](#)] [[PubMed](#)]

33. Mullica, D.F.; Oliver, J.D.; Milligan, W.O.; Hills, F.W. Ferrous hexacyanocobaltate dodecahydrate. *Inorg. Nucl. Chem. Lett.* **1979**, *15*, 361–365. [[CrossRef](#)]
34. Adak, S.; Daemen, L.L.; Hartl, M.; Williams, D.; Summerhill, J.; Nakotte, H. Thermal expansion in 3d-metal Prussian Blue Analogs—A survey study. *J. Solid State Chem.* **2011**, *184*, 2854–2861. [[CrossRef](#)]
35. Aquilanti, G.; Giorgetti, M.; Dominko, R.; Stievano, L.; Arçon, I.; Novello, N.; Olivi, L. Operando characterization of batteries using x-ray absorption spectroscopy: Advances at the beamline XAFS at synchrotron Elettra. *J. Phys. D Appl. Phys.* **2017**, *50*, 074001. [[CrossRef](#)]
36. Giorgetti, M.; Mignani, A.; Aquilanti, G.; Conti, P.; Fehse, M.; Stievano, L. Structural and electronic studies of metal hexacyanoferrates based cathodes for Li rechargeable batteries. *J. Phys. Conf. Ser.* **2016**, *712*, 012127. [[CrossRef](#)]
37. De Juan, A.; Jaumot, J.; Tauler, R. Multivariate Curve Resolution (MCR). Solving the mixture analysis problem. *Anal. Methods* **2014**, *6*, 4964–4976. [[CrossRef](#)]
38. Berrettoni, M.; Giorgetti, M.; Zamponi, S.; Conti, P.; Ranganathan, D.; Zanutto, A.; Saladino, M.L.; Caponetti, E. Synthesis and characterization of nanostructured cobalt hexacyanoferrate. *J. Phys. Chem. C* **2010**, *114*, 6401–6407. [[CrossRef](#)]
39. Giorgetti, M.; Aquilanti, G.; Ciabocco, M.; Berrettoni, M. Anatase-driven charge transfer involving a spin transition in cobalt iron cyanide nanostructures. *Phys. Chem. Chem. Phys.* **2015**, *17*, 22519–22522. [[CrossRef](#)] [[PubMed](#)]
40. Hayakawa, K.; Hatada, K.; D'Angelo, P.; Della Longa, S.; Natoli, C.R.; Benfatto, M. Full quantitative multiple-scattering analysis of X-ray absorption spectra: Application to potassium hexacyanoferrate(II) and-(III) complexes. *J. Am. Chem. Soc.* **2004**, *126*, 15618–15623. [[CrossRef](#)] [[PubMed](#)]
41. Bianconi, A.; Dell'Araccia, M.; Durham, P.J.; Pendry, J.B. Multiple-scattering resonances and structural effects in the x-ray-absorption near-edge spectra of Fe^{II} and Fe^{III} hexacyanide complexes. *Phys. Rev. B* **1982**, *26*, 6502–6508. [[CrossRef](#)]
42. Kosugi, N.; Yokoyama, T.; Kuroda, H. Polarization dependence of XANES of square-planar Ni(CN)₄²⁻ ion. A comparison with octahedral Fe(CN)₆⁴⁻ and Fe(CN)₆³⁻ ions. *Chem. Phys.* **1986**, *104*, 449–453. [[CrossRef](#)]
43. Giorgetti, M.; Berrettoni, M. Structure of Fe/Co/Ni hexacyanoferrate as probed by multiple edge X-ray absorption spectroscopy. *Inorg. Chem.* **2008**, *47*, 6001–6008. [[CrossRef](#)] [[PubMed](#)]
44. Hannauer, J.; Scheers, J.; Fullenwarth, J.; Fraisse, B.; Stievano, L.; Johansson, P. The Quest for Polysulfides in Lithium-Sulfur Battery Electrolytes: An Operando Confocal Raman Spectroscopy Study. *Chem. Phys. Chem.* **2015**, *16*, 2755–2759. [[CrossRef](#)] [[PubMed](#)]
45. Rebuffi, L.; Plaisier, J.R.; Abdellatif, M.; Lausi, A.; Scardi, A.P. Mx: A synchrotron radiation beamline for X-ray diffraction line profile analysis. *Z. Anorg. Allg. Chem.* **2014**, *640*, 3100–3106. [[CrossRef](#)]
46. Rodríguez-Carvajal, J. Recent advances in magnetic structure determination by neutron powder diffraction. *Phys. B Phys. Condens. Matter* **1993**, *192*, 55–69. [[CrossRef](#)]
47. Yao, M.; Kuratani, K.; Kojima, T.; Takeichi, N.; Senoh, H.; Kiyobayashi, T. Indigo carmine: An organic crystal as a positive-electrode material for rechargeable sodium batteries. *Sci. Rep.* **2014**, *4*, 3650. [[CrossRef](#)] [[PubMed](#)]
48. Momma, K.; Izumi, F. VESTA 3 for three-dimensional visualization of crystal, volumetric and morphology data. *J. Appl. Crystallogr.* **2011**, *44*, 1272–1276. [[CrossRef](#)]
49. Ravel, B.; Newville, M. ATHENA, ARTEMIS, HEPHAESTUS: Data analysis for X-ray absorption spectroscopy using IFEFFIT. *J. Synchrotron Radiat.* **2005**, *12*, 537–541. [[CrossRef](#)] [[PubMed](#)]
50. Filipponi, A.; Di Cicco, A.; Natoli, C.R. X-ray-absorption spectroscopy and n-body distribution functions in condensed matter. I. Theory. *Phys. Rev. B* **1995**, *52*, 15122–15134. [[CrossRef](#)]
51. Filipponi, A.; Di Cicco, A. X-ray-absorption spectroscopy and n-body distribution functions in condensed matter. II. Data analysis and applications. *Phys. Rev. B* **1995**, *52*, 15135–15149. [[CrossRef](#)]
52. Giorgetti, M.; Berrettoni, M.; Filipponi, A.; Kulesza, P.J.; Marassi, R. Evidence of four-body contributions in the EXAFS spectrum of Na₂Co[Fe(CN)₆]. *Chem. Phys. Lett.* **1997**, *275*, 108–112. [[CrossRef](#)]
53. Giorgetti, M.; Guadagnini, L.; Tonelli, D.; Minicucci, M.; Aquilanti, G. Structural characterization of electrodeposited copper hexacyanoferrate films by using a spectroscopic multi-technique approach. *Phys. Chem. Chem. Phys.* **2012**, *14*, 5527–5537. [[CrossRef](#)] [[PubMed](#)]

54. Hedin, L.; Lundqvist, B.I.; Lundqvist, S. Local exchange-correlation potentials. *Solid State Commun.* **1971**, *9*, 537–541. [[CrossRef](#)]
55. Krause, M.O.; Oliver, J.H. Natural widths of atomic K and L levels, K α X-ray lines and several K L L Auger lines. *J. Phys. Chem. Ref. Data* **1979**, *8*, 329–338. [[CrossRef](#)]



© 2018 by the authors. Licensee MDPI, Basel, Switzerland. This article is an open access article distributed under the terms and conditions of the Creative Commons Attribution (CC BY) license (<http://creativecommons.org/licenses/by/4.0/>).